Local gas-liquid hold-up and interfacial area via light sheet and image analysis

A. Busciglio, F. Scargiali, F. Grisafi, A. Brucato
Università degli Studi di Palermo; Dipartimento di Ingegneria Chimica, dei Processi e dei Materiali;
Viale delle Scienze, Ed. 6, 90128, Palermo, Italy, tel: +3909123863715,
e-mail: a.busciglio@dicpm.unipa.it

Abstract. Particle Image Velocimetry techniques coupled with advanced Image Processing tools are receiving an increasing interest for measuring flow quantities and local bubble-size distributions in gas-liquid contactors.

In this work, an effective experimental technique for measuring local gas hold-up and interfacial area, as well as bubble size distribution, is discussed. The technique, hereafter referred to as Laser Induced Fluorescence with Shadow Analysis for Bubble Sizing (LIF-SABS) is based on laser sheet illumination of the gas-liquid dispersion and synchronized camera, i.e. on equipment typically available within PIV set-ups. The liquid phase is made fluorescent by a suitable dye, and an optical filter is placed in front of the camera optics, in order to allow only fluoresced light to reach the camera CCD. In this way bubbles intercepted by the laser sheet are clearly identified thanks to the neat shade resulting in the images. This allows excluding from subsequent analysis all bubbles visible in the images but not actually intercepted by the laser sheet, so resulting in better spatial resolution and data reliability.

When trying to analyze image information the problem arises that bubble sizes are generally underestimated, due to the fact that the laser sheet randomly cuts bubbles over non-diametrical planes, leading to an apparent bubble size distribution even in the ideal case of single sized bubbles. Clearly in the case of bubbles with a size distribution the experimental information obtained is affected by the superposition of effects. A statistical correction for estimating local gas hold-up and specific interfacial area from relevant apparent data as obtained by laser sheet illumination and image analysis is discussed and applied to preliminary experimental data obtained in a gas-liquid stirred vessel.

Keywords. Gas-Liquid flows, Bubbles, BSD, LIF-SABS, local hold-up, interfacial area

INTRODUCTION

Gas-liquid contactors are widely employed as reactors and bio-reactors in the process industry. Gas-liquid mass transfer is a common rate-determining step in these apparatuses. Local mass transfer areas depend on bubble size and concentration, and vary notably from place to place even in small stirred tanks (Calderbank, 1958; Sridhar and Potter 1980; Barigou and Greaves 1992, 1996). Mass transfer area is obtained most reliably from local gas hold-up and bubble size distribution (BSD). A thorough review of measuring techniques in gas liquid contactors can be found in Boyer et al. (2002).

Particle Image Velocimetry techniques (PIV) have been used in recent years for velocity field measurements in gas-liquid systems (Montante et al. 2007, Khopkar et al. 2003, Aubin et al. 2004). One of the most innovative application of PIV setups is the measurement of BSD (Spicka et al. 2001, Liu Z. et al. 2005; Laakkonen et al. 2005). As a matter of fact, PIV apparatuses, apart from providing information on the flow and turbulence quantities in gas-liquid systems, may be employed for other measurements, taking advantage of the possibility of isolating a well known volume of the systems. This, in conjunction with advanced Digital Image Processing Techniques may in principle provide simultaneous measurements of both BSD and local gas hold-up.

In this work an advanced technique aimed at measuring local gas hold-up and interfacial area, is proposed. The technique is based on laser sheet illumination and synchronized camera (i.e. on typical PIV equipment) in conjunction with a fluorescent liquid phase and a purposely developed image analysis procedure. Preliminary data obtained in a stirred gas-liquid dispersion that confirm the technique viability and reliability are also presented.

EXPERIMENTAL SETUP

Experiments were carried out in a flat bottomed, fully baffled cylindrical vessel (diameter $T = 0.19\ m$, stirred by a standard Rushton turbine ($D = T/3$) offset by $T/3$ from vessel bottom. The liquid phase was deionised water in which a fluorescent dye (Rhodamine-B) had been dissolved. The gas phase (air) was supplied through a *6 mm ID* open-ended pipe, centrally placed *10 mm* below the turbine.

The gas-liquid dispersion was illuminated by a pulsed laser sheet (Nd-Yag, *50 mW* per pulse, New Wave Research "Solo III", wavelength equal to *532 nm*). The resulting images were acquired by a high sensitivity digital camera (1280×1024 pixel, Hamamatsu) connected to a Dantec FlowMap 1500 synchronization/acquisition unit.

The cylindrical vessel was immersed in a water through in order to minimize optical distortions. A band-pass filter centred on the wavelength of fluoresced light (*570 nm*) was placed in front of the camera in order to allow only this light to reach the CCD. On the basis of preliminary tests, an optimal Rhodamine concentration of *0.5 mg/l* was adopted. Higher concentrations result in too strong laser sheet attenuation, and therefore a troublesome non-uniformity in the tank illumination level, while lower concentrations give rise to excessively dark images. Gas flow rate of $Q_g = 0.3\ lt/min$ and at a rotational speed of *300 rpm,* well above the critical speed for complete dispersion, were adopted for this work.

IMAGE PROCESSING

A typical image of the lower part of the vessel obtained by the above described apparatus is shown in Fig.1a, where the right border coincides with the vessel axis and the impeller region is digitally shielded in order to avoid spurious results in the subsequent image analysis. The laser sheet entered from the left side of the image and travelled towards the right side on a vertical plane at 45° between subsequent baffles. All the light observable in Fig.1a is that re-emitted by the fluorescent dye, that practically turns the laser sheet into a planar fluoresced-light source.

In this image gas bubbles can be clearly observed. Some are "dark bordered" and are clearly placed in front of the light sheet, while others are "white bordered" and may be entirely beyond the light plane or actually struck by the light plane. The latter are however easily identified as they are the only ones that give rise to a neat straight "shadow" in the image, caused by the fact that the laser light intercepted is diverted in many directions and fails to excite the dye on the light path rear the bubble, as can be appreciated in Fig.1a. It may be worth noting that the vertical dark and white lines in Fig.1a is are baffle borders.

On this basis, a suitable imaging technique can be developed to unequivocally identify in-plane bubbles (those white-bordered and associated with the straight shadows) and discard all other bubbles from subsequent analysis, i.e. the measurement of dispersion properties as gas hold-up and bubble size distribution, sharply pertaining to the investigated plane.

In order to improve the automatic recognition of the in-plane bubbles, some image processing is advisable, aimed at enhancing white borders and bubble "shadows".

The first processing step adopted in this work was background subtraction from the original image. The average background luminance in the presence of gas bubbles was found to be quite

different from that obtained in absence of gas, and lead to rather noisy images if adopted. Better results were obtained using time-averaged images of the gassed system as the background image. In this way, given the quite low gas flow rates investigated and correspondingly low gas hold-ups, the noise introduced in the background image is of the order of 1% of the image signal.

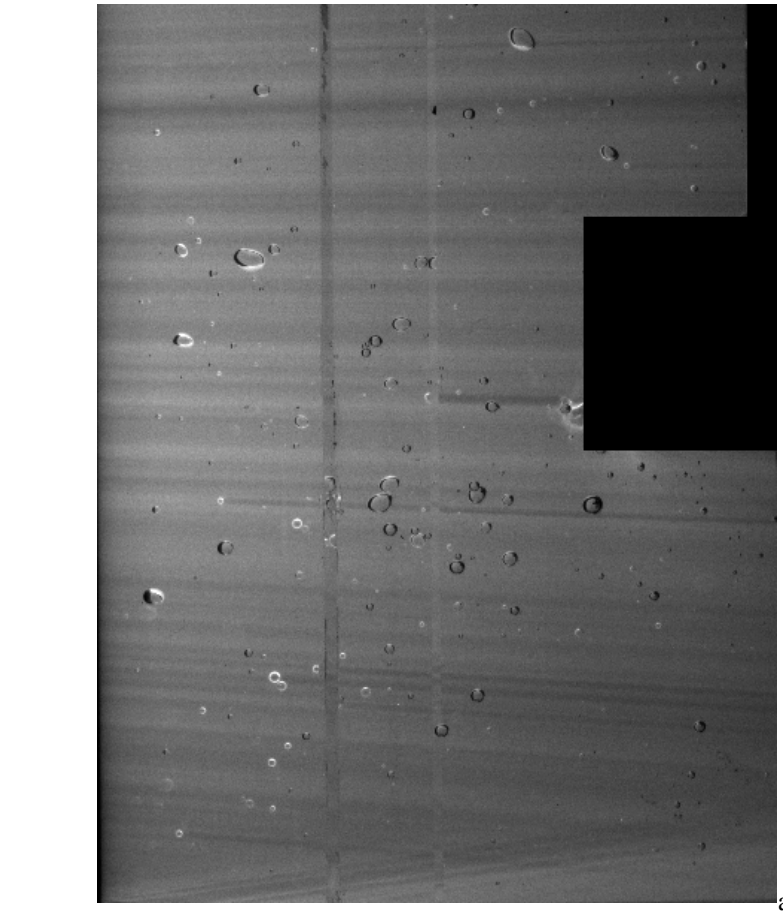

a)

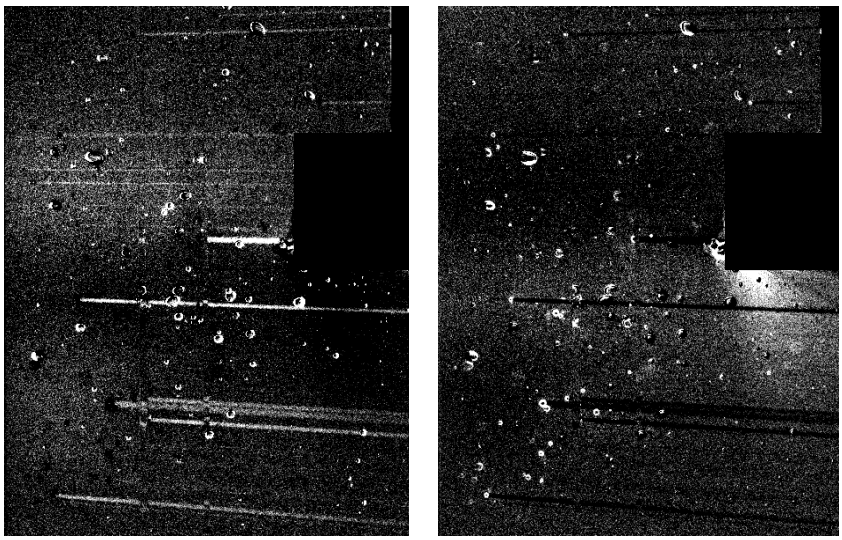

b) c)

Figure 1 From left to right, a) typical raw image of the vessel, b) absolute difference between raw and background images, c) simple difference between raw and background images.

Shadows have generally a luminance value smaller than the background image: hence, by subtracting the raw image from background, the darkest pixel in the raw image are enhanced,

therefore making shadows very evident, as it can be seen in Fig.1b. This last is therefore best suited for shadows identification. Conversely, bubble white borders have a luminance value greater than the background image hence the simple difference between the raw image and the background will put them in evidence (Fig.1c). Simple difference images are therefore best suited to exactly identify bubble size and position, once their in-plane position has been ascertained by the previous shadows elaboration.

Though not strictly needed, after trial and error attempts, improvement in bubble automatic identification was obtained by further image processing. In particular images like Figs.1b-c underwent 2-dimensional Wiener filtering (a pixelwise adaptive method based on statistics estimated from a local neighbourhood of each pixel. After this transformation, different image processing routes were followed. In particular, the enhanced-shadow images underwent a morphological transform by which most of the round objects (i.e. dark bordered bubbles in the raw image) were deleted, in order to isolate the long straight shadows. The final result of this transformation is reported in Fig.2a. The enhanced-bubble image underwent morphological filling of closed round objects, binarization and watershed transform to separate overlapped bubbles and scattered light around bubbles. The final results of this processing are shown in Fig.2b (before binarization) and Fig.2c (after binarization and watershed transforms).

For shadows automatic recognition in Fig.2a no standard algorithms for straight lines (for instance based on image Fourier transforms) could be employed, because of: i) the diffuse border of the shadows, ii) the non-uniform intensity of the shadows and iii) the fact that the shadows are not exactly parallel to each other. However, as the laser behaves as a pointwise source, bubble shadows concur to the same point, covering a certain angle range with respect to the horizontal direction. Hence the shadow recognition algorithm employed was based on the only invariant property of the shadows themselves, i.e. the common passage through the laser emission point.

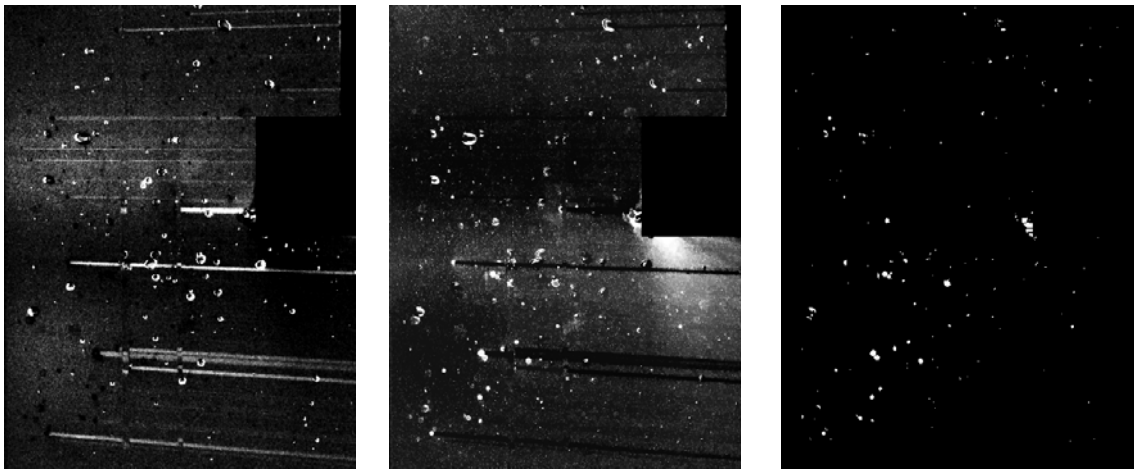

a) b) c)

Figure 2 From left to right, a) enhanced shadow image, b) enhanced bubble image, c) final binarized bubble image.

In particular, since the emission point and the range of angles (with respect to the horizontal plane) included in the image are known, it is possible to isolate only the pixel sequences lying on each possible laser ray. Each of these pixel sequences behaves differently whether it includes a shadow or not. Namely, the average value of pixel luminance will be larger when a bright shadow is involved, while a smaller mean value will be observed in the other case. Moreover, some care must be taken to recognize long (projected by near wall bubbles) and short shadows (projected by near centre bubbles). This is achieved by simply dividing each possible ray and computing the overall mean value, the double of the mean value of the last half, the forth of the mean value of the last

quarter, the eighth of the mean value of the last eight. By summing these values, for each ray an output value is obtained, as reported in Fig.3a.

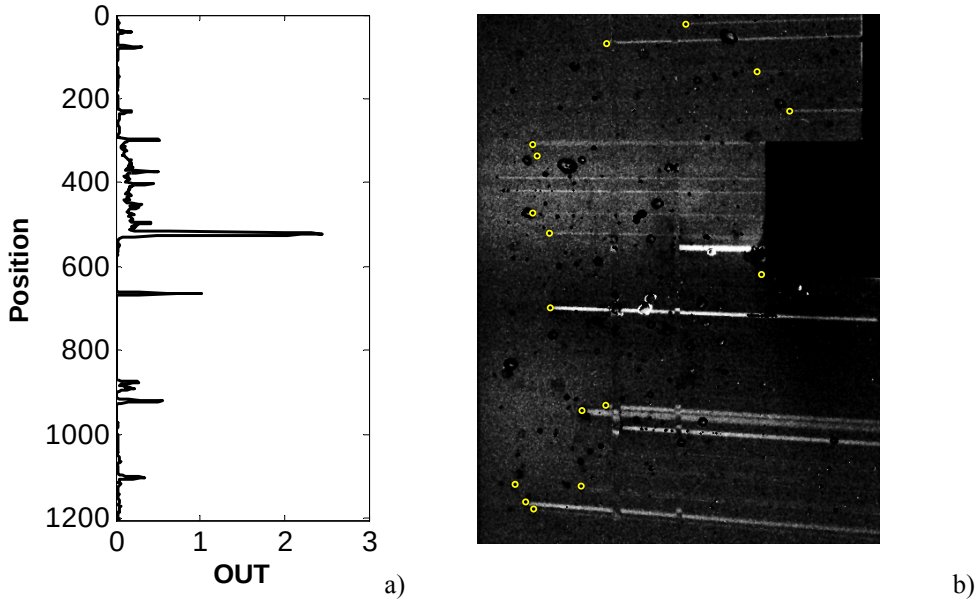

Figure 3 a) Output function compared with enhanced shadow image. b) identified in plane bubbles

As it can be seen, the output function is actually very effective in suppressing noise and making shadow identification very neat. The peaks, i.e. shadows (and in turn in-plane bubbles) can therefore be automatically. The identification algorithm is based on the simple evidence that along each selected ray a neat change of luminance must be found where the in-plane bubble is encountered. In Fig.3b, the result of this procedure is shown. It is worth noting that most of the in-plane bubbles are correctly selected. Clearly, the technique can further be improved by means of more advanced image analysis technique for noise suppression or more efficient algorithms for in plane bubbles identification.

Remarkably, the final output of the technique here proposed is a binarized phase matrix $\Phi(x,y)$, in which pixels belonging to in-plane gas phase are set to one and all other pixels are set to zero. For each bubble present in the image, its area, equivalent diameter and centroid coordinates can be computed and stored. This kind of information can be used for the assessment of typical gas-liquid dispersion properties such as local bubble size distribution, local specific interfacial area and local gas hols up, provided that some data elaboration is performed to transform planar data into relevant volumetric data.

DATA PROCESSING

As a result of image processing, the size and position of bubbles intercepted by the laser sheet are assessed. The intercept sizes are obviously different from each other, so that a "visible intercept size distribution", *VISD(l)*, is practically assessed. This is related to the actual bubble size distribution *BSD(r)* but in general does not coincide with it, as the laser sheet intercepts bubbles over non diametrical planes at random distances from bubble center. It may be concluded that the *VISD(l)* is bound to underestimate the actual *BSD(r)* to some extent, and the need clearly arises for devising ways for transforming measured *VISD*s into the relevant (actual) *BSD*s. The above defined *VISD(l)* quantifies the likelihood of finding intercepts of size *l* among the whole set of intercept chords, and is determined by the following factors:

- the actual bubble size distribution *BSD(r)*;

- the *conditional probability function P(l|r)* that gives the likelyhood of intercepting a chord of length *l* from a number of bubbles all having a radius equal to *r*;
- the *biased probability* $P_B(r)$, that describes the probability of an *r* sized bubble of being sampled when bubbles are uniformly distributed in the system. The biased probability accounts for the circumstance that the sampling device is more likely to sample larger bubbles than smaller ones.

These three factors are independent of each other.

The relationship between *BSD*s and relevant intercept distributions (*VISD*s) has been widely investigated in the past because of its relevance to multiphase dispersed flow measurements. Such relationships are in fact needed when needle probes are used to investigate bubble properties such as size or velocity in both gas-solid flows (Gunn and Al-Doori, 1985; Clark and Turton, 1988; Liu and Clark, 1995; Clark et al., 1996; Liu et al., 1996, 1998) and gas-liquid flows (Herringe and Davis, 1976; Hobbel et al., 1991). A number of works can be found on the techniques needed to infer the bubble (particle or droplet) size distribution from chord length distributions as directly obtained by specific instruments, based on fixed or rotating laser beams, such as the Lasentec Par-Tec 300 (Simmons et al., 1999; Langston et al., 2001) or the Lasentec FBRM (Ruf et al., 2000; Wynn, 2003; Worlitschek et al., 2005; Li and Wilkinson, 2005; Li et al., 2005).

In general, the *VISD(l)* is related to the above discussed probability functions by the following equation:

$$VISD(l) = \int_o^\infty P(l \mid r) P_B(r) BSD(r) dr \tag{1}$$

The analytical form of cumulative conditional probability *P(l|r)* has been derived for different bubble shapes when pierced by a needle probe (Clark and Turton, 1988) or obtained by means of Focused Beam Reflectance Measurement (Ruf et al., 2000, Li and Wilkinson, 2005). For the case of zero thickness planar probes (i.e. in the present case of laser plane, Busciglio et al., 2010a), it can be demonstrated that:

$$P(l \mid r) = \begin{cases} \dfrac{l}{r^2 \sqrt{1 - \left(\dfrac{l}{r}\right)^2}} \Leftrightarrow l \le r \\ 0 \Leftrightarrow l > r \end{cases} \tag{2}$$

$$cP(l \mid r) = \begin{cases} 1 - \sqrt{1 - \left(\dfrac{l}{r}\right)^2} \Leftrightarrow l \le r \\ 1 \Leftrightarrow l > r \end{cases} \tag{3}$$

The typical thickness of laser sheets in PIV apparatuses is of the order of few millimeters and is therefore comparable with the size of bubbles in most gas-liquid systems. Therefore the effect of laser sheet thickness on bubble properties measurement must be properly accounted for.

In the case of finite-thickness light sheet (thick light sheets), the ratio between bubble radius and light-sheet thickness may be included as a new variable when assessing the statistical distributions of apparent radii. A thick light sheet intersecting gas bubbles may give rise to one or two detectable intercept radii, as depicted in Fig.4. The light sheet will result into detectable intercept(s) if the

distance between the light median plane and bubble centre is smaller or equal to the sum of the bubble radius r and half of the light sheet thickness w_{ls}, as can be seen in Fig.4, case A. With the above presented LIF-SABS technique, only the largest intercept is neatly measured by image analysis. The technique is somewhat similar to that proposed by Chung et al., (2009), but a completely different out-of-plane bubble discarding algorithm is proposed.

With this detection technique, the way in which the light sheet cuts the gas bubble gives rise to different apparent radii: if only one of the light sheet boundaries intersects the bubble, only one intercept radius is detectable and no ambiguity is incurred (case B in Fig.4); when both light sheet boundaries intersect the bubble in such a way that intercepts lie on the same side with respect to the bubble diametrical plane, two intercept radii may be detected (case C in Fig.4); experimental experience shows that under such circumstances the external boundary is easier to detect than the internal one and gives rise to minor sensitivity to image processing parameters, such as binarization thresholding; the former is therefore adopted as the nominal intercept radius in such cases. Finally, when both light sheet boundaries intersect the bubble in such a way that intercepts lie on different sides of bubble centre (case D in Fig.4) then the visible bubble boundary coincides with the diametrical plane. Notably, if w_{ls} is larger than bubble size (case E in Fig.4), there is a chance for the bubble to be entirely within the thick laser sheet.

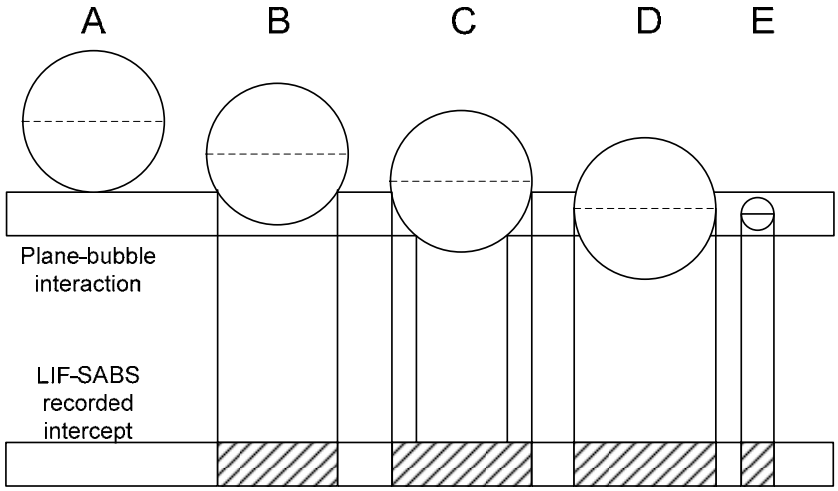

Figure 4 Intercept radii (dashed lines are the bubble diametrical planes).

On this basis, it is clear that the probability of finding apparent radii equal to the effective bubble radius increases with w_{ls}/r, since the probability of finding the diametrical plane of the bubble inside the light sheet increases in turn. The analytical expression for $cP(l|r)$ in the case of thick light sheet can be obtained with a procedure similar to that used for Eqns.2-3 (Busciglio et al., 2010a), with the only exception that part of the planes adopted for the bubble cut give rise to an intercept radius exactly equal to r. In particular, all cut planes at a distance from bubble center lower than half of the light sheet thickness will result in an intercept radius equal to r. On this basis, the fraction of intercept planes giving rise to visible intercept radii equal to r, i.e. the probability P_d of the light sheet to include the diametrical plane is given by:

$$P_d = \frac{w_{ls}}{2r + w_{ls}} \tag{4}$$

Conversely, all others cut planes will give rise to a statistical distribution of visible intercept radii identical to that for thin light sheet (Eqns.2-3) multiplied by the relevant fraction of planes, thus resulting into the following equation:

$$cP(l \mid r) = \begin{cases} (1 - P_d)\left[1 - \sqrt{1 - \left(\frac{l}{r}\right)^2}\right] \Leftrightarrow l \le r \\ 1 \Leftrightarrow l > r \end{cases} \tag{5}$$

The discontinuity at $l = r$ in Eqn.5 derives from the above mentioned considerations on the probability of including the bubble diametrical plane into the light sheet.

The dependence of the biased probability $P_B(r)$ on r^2 in the case of punctual probes was firstly addressed on the basis of bubble geometrical properties by Herringe and Davis (1976), and subsequently formalized by Liu and Clark (1995). In the case of planar probes, if an r sized bubble is considered in a physical space having length equal to λ, and is cut by a light sheet having thickness equal to w_{ls}, with positions equidistributed over the length λ, the probability of the light sheet to intercept the bubble is given by:

$$P_B = \frac{2r + w_{ls}}{\lambda} \tag{6}$$

Interfacial area and holdup

The overall gas hold-up in gas liquid dispersions is simply defined as the ratio between gas phase volume and overall volume:

$$\varepsilon = \frac{\int_V dV_{gas}}{\int_V dV_{gas} + \int_V dV_{liq}} \tag{7}$$

Conversely, a local gas hold-up is more difficult to define: in fact, when infinitesimal volumes dV are considered, the instantaneous local hold-up is either *0* or *1* depending on the fact that the point considered is occupied by the liquid or the gas phase respectively. Therefore the instantaneous local hold up can be expressed by defining an instantaneous phase indicator

$$\Phi(x,y) = \begin{cases} 1 \Leftrightarrow (x,y) \in V_{gas} \\ 0 \Leftrightarrow (x,y) \notin V_{gas} \end{cases} \tag{8}$$

The average instantaneous hold-up over volume V and relevant time average may be therefore written as:

$$\varepsilon_{av} = \frac{1}{V}\int_V \Phi\, dV \tag{9}$$

and by defining the time averaged local hold-up as:

$$\overline{\varepsilon_{loc}} = \frac{1}{T}\int_T \Phi\, dt \tag{10}$$

This last clearly abides by the property that:

$$\overline{\varepsilon_{av}} = \frac{1}{V}\int_V \overline{\varepsilon_{loc}}\, dV \tag{11}$$

Hence, in the case of zero thickness laser sheet, if N time-equispaced phase matrices are taken, the time averaged local gas hold-up can be simply computed in each image pixel:

$$\varepsilon_a(x,y) = \frac{1}{N}\sum \Phi(x,y) \tag{12}$$

A similar approach can be adopted to estimate the gas liquid interfacial area. Computing the gas-liquid interface perimeter observable in a λ by λ square in the phase matrix is fairly straightforward. This information may be averaged over N images to get a time averaged perimeter in the same area and by dividing it by λ^2 a quantity akin to specific interfacial area is obtained. Let us call it *apparent interfacial area*:

$$a_{i,a} = \frac{1}{N\lambda^2}\sum p_i \tag{13}$$

where p_i is the gas-liquid perimeter found in each image in the above defined region. Equations 12-13 defines in practice the quantity that are experimentally accessed by the LIF-SABS technique. However, the relation with actual (volumetric) specific interfacial area is not as plain as in the case of gas hold-up, in which volumetric and apparent phase fraction coincide if an infinitesimally thin slice is considered. The fundamentals of this problem were stated in the Buffon's needle problem (Buffon, 1777), whose solution was the start of modern statistical geometry and stereology (Mandarim De Lacerda, 2003; Stroeven and Hu, 2006). It is universally accepted that the following relation exists between apparent and actual specific interfacial area, when bubbles of any shape intercepted by infinitesimally thin light sheets are considered (see for instance Russ and Dehoff, 1999):

$$a_{i,a} = \frac{4}{\pi} a_i \tag{14}$$

In addition to these difficulties, the laser sheet thickness (that in PIV apparatuses is generally thick, *i.e.* comparable with bubble size) must be accounted for. In fact, the thicker the laser sheet, the greater the probability of including the diametrical plane into the light sheet. Moreover, knowledge of the gas-to-dispersion volume ratio depends on the way in which bubbles are cut. In thick laser sheet, the gas-to-dispersion volume ratio can be approximated by considering cylindrical intercepts having radius equal to the recorded intercept size and height equal to the laser sheet thickness. This identification clearly introduces an overestimation of both gas hold up and specific interfacial area.

It is however possible to correct such measurements by means of statistical analysis under the hypothesis of spherical bubbles. Two correction factor can be defined for transforming the apparent hold-up (above defined) and specific interfacial area into the relevant volumetric values.

$$f_\varepsilon = \frac{\varepsilon}{\varepsilon_a} \tag{15}$$

$$f_{a_i} = \frac{a_{i,a}}{a_i} \tag{16}$$

As mentioned earlier, the apparent volume and surface of the bubble can be expressed by computing the gas volume and area a cylinder with base radius equal to the measured intercept length l and height equal to the laser sheet thickness w_{ls}.

On this basis, the hold-up correction factor can be immediately expressed as a function of the actual radii data set and the intercept data set.

$$\frac{\varepsilon}{\varepsilon_a} = \frac{\sum 4\pi r^3 / 3}{\lambda^3} \frac{w_{ls}\lambda^2}{\sum \pi l^2 w_{ls}} = \frac{4}{3\lambda} \frac{\sum r^3}{\sum l^2} \tag{17}$$

It is possible to substitute the sums in Eqn.17 with the relevant distribution moments (in the followings, all integrals are meant as definite integrals between *0* and *1*, unless otherwise indicated):

$$\frac{\varepsilon}{\varepsilon_a} = \frac{4}{3\lambda} \frac{\int r^3 BSD(r)dr}{\int l^2 VISD(l)dl} = \frac{4}{3\lambda} \frac{\int r^3 BSD(r)dr}{\iint l^2 P_B(r)P(l \mid r)BSD(r)drdl} \tag{18}$$

and by introducing Eqns.5 and 6 by simple manipulation (reported in Busciglio et al., 2010b) the following result is obtained:

$$f_\varepsilon = \frac{1}{1 + \frac{3w_{ls}}{4r_{32}}} \tag{19}$$

It is worth noting that is not possible to obtain a correction factor completely independent of actual bubble size distribution. Nevertheless, it has been shown that the correction factor only depends on the ratio between the known laser sheet thickness and the average bubble radius r_{32}, independently of BSD shape.

A similar procedure can be adopted to express the actual and apparent interfacial area as a function of the actual radii data set and the intercept data set, and the relevant correction factor

$$a_i = \frac{S}{V_g}\frac{V_g}{V} = \frac{\sum 4\pi r^2}{\sum 4\pi r^3 / 3} = \frac{3}{r_{32}}\varepsilon \tag{20}$$

$$a_{i,a} = \frac{S_a}{V_{ga}}\frac{V_{ga}}{V_a} = \frac{\sum 2\pi l w_{ls}}{\sum 2\pi l^2 w_{ls}} = \frac{2}{l_{21}}\varepsilon_a \tag{21}$$

$$f_{a_i} = \frac{a_{i,a}}{a_i} = \frac{3}{2}\frac{\varepsilon}{\varepsilon_a}\frac{l_{21}}{r_{32}} = \frac{3}{2}f_\varepsilon \frac{l_{21}}{r_{32}} \tag{22}$$

Since the correction factor f_ε has already been derived, only the value of the ratio l_{21}/r_{32} is needed in order to compute f_{ai}, as shown by Eqn.22. Again, it is necessary to compute the average intercepts as the ratio between relevant distribution moments. By means of the same substitutions and manipulation of Eqn.18, it is possible to compute different ratios between *VISD* and *BSD* moments:

$$\frac{l_{10}}{r_{21}} = \frac{\frac{\pi}{2} + \frac{w_{ls}}{r_{21}}}{2 + \frac{w_{ls}}{r_{10}}} \tag{23}$$

$$\frac{l_{21}}{r_{32}} = \frac{\frac{4}{3} + \frac{w_{ls}}{r_{32}}}{\frac{\pi}{2} + \frac{w_{ls}}{r_{21}}} \tag{24}$$

$$\frac{l_{32}}{r_{43}} = \frac{\frac{3\pi}{8} + \frac{w_{ls}}{r_{43}}}{\frac{4}{3} + \frac{w_{ls}}{r_{32}}} \tag{25}$$

On the basis of Eqns.19, 22, and 24 the following expression can be derived for the correction factor f_{ai} :

$$f_{a_i} = \frac{2}{\frac{\pi}{2} + \frac{3w_{ls}}{4r_{21}}} \tag{26}$$

Equation 26 shows that once again it is not possible to obtain a correction factor completely independent of bubble size distribution. Nevertheless, it has been shown that the correction factor only depends on the ratio between the known laser sheet thickness and average bubble radius r_{21}, (instead of r_{32}).

Both correction factors are fully consistent with well known results in the field of stereology, *i.e.* when thin light plane is considered, f_ε tends to one and f_{ai} tends to $4/\pi$.

In order to validate the method and quantitatively exemplify the extent of the dependence of results on *BSD*, Monte Carlo simulations providing pseudo-experimental intercept information were run in relation to several input *BSD*s. The pseudo-experimental information on bubble intercepts so obtained was then processed in order to compare the global hold-up and specific interfacial area with relevant intercept measurements.

It must be emphasized that the laser sheet thickness is typically known from experiment, but the same does not hold true for the r_{32} and r_{21} values needed for computing the correction factors, because only intercept sizes are directly available from image analysis. On the other hand, Eqns.23 and 24 link r_{32} and r_{21} to l_{21} and l_{10} respectively. These results can be used to approximate the correction factors by only using functions of experimentally available quantities. In particular, it is possible to observe that limits of Eqns.23 and 24 can be computed for w_{ls} approaching zero and infinite. This will result in two ”limiting” (thou not bounding) values for the proportionality between r_{32} and l_{21} (Eqn.28), and for the proportionality between r_{21} and l_{10} (Eqn.27).

$$l_{10} = \left(\frac{\pi}{4} \div \frac{r_{10}}{r_{21}}\right) r_{21} \tag{27}$$

$$l_{21} = \left(\frac{8}{3\pi} \div \frac{r_{21}}{r_{32}}\right) r_{32} \tag{28}$$

As a simple (but reasonably realistic) case, by substituting the lower bounding values of Eqns.27 and 28 into Eqns. 19 and 26, the approximated correction factors can be computed as follows:

$$f_{\varepsilon} \cong \frac{1}{1+0.849\dfrac{3w_{ls}}{4l_{21}}} \tag{29}$$

$$f_{a_i} = \frac{2}{\dfrac{\pi}{2}+0.785\dfrac{3w_{ls}}{4l_{10}}} \tag{30}$$

The reliability of such simplified theoretical correction curve was extensively tested with Monte Carlo simulation in Busciglio et al. (2010). With these simple yet effective corrections, the required *VISD* moments and the relevant correction factors for hold-up and interfacial area can be calculated for each region of the vessel image, and used for direct measurement of local gas hold-up and interfacial area from PIV images.

RESULTS

The procedure viability was checked by processing 2000 images obtained with the previously described experimental apparatus. It may be worth noting that collecting the 2000 images involved only few minutes of experimentation while much longer times were needed for the subsequent image processing. As a matter of fact, about 6 CPU hours were required on a Core 2 duo running at 2.33 GHz. It may be worth noting that for this type of computation parallelization is very easily accomplished by simply subdividing the total number of images to be processed among different jobs running on each available CPU.

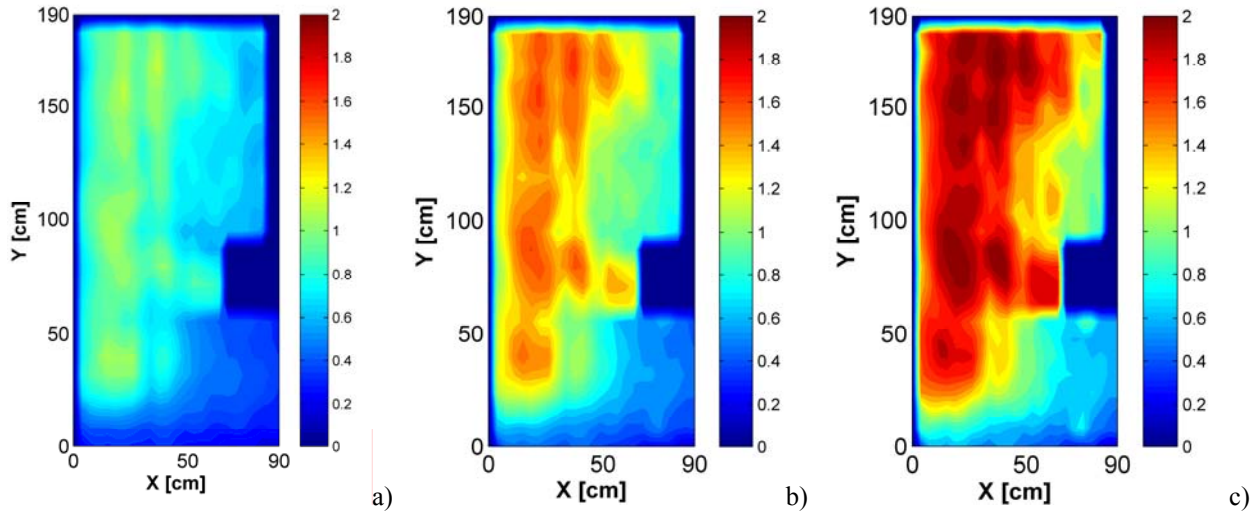

Figure 5 a) L_{10} map. b) L_{21} map. c) L_{32} map.

In Fig.5 data on local average intercept sizes are reported. In particular by merging results obtained over 50*50 pixel areas the local bubble size maps for L_{10}, L_{21} and L_{32} in Fig.5 were obtained. The relevant moments as obtained from an overall average over the entire maps were $L_{10} = 0.78\ mm$, $L_{21} = 1.23\ mm$, $L_{32} = 1.67\ mm$ respectively.

As it concerns gas hold-up, although in principle an extremely detailed information can be collected (an average hold-up datum in each of the 1280*1024 pixel locations) once again the 2000 images analysed were insufficient for getting statistically stable results and some data merging was

needed to obtain meaningful results. In particular by merging results obtained over 50*50 pixel areas the local gas hold-map map shown in Fig.7a was obtained. Notably, the local correction factor reported in Eqn.29 must be applied pointwise to the map reported in Fig.6a, to infer the actual volumetric hold-up map. This latter is reported in Fig.6b.

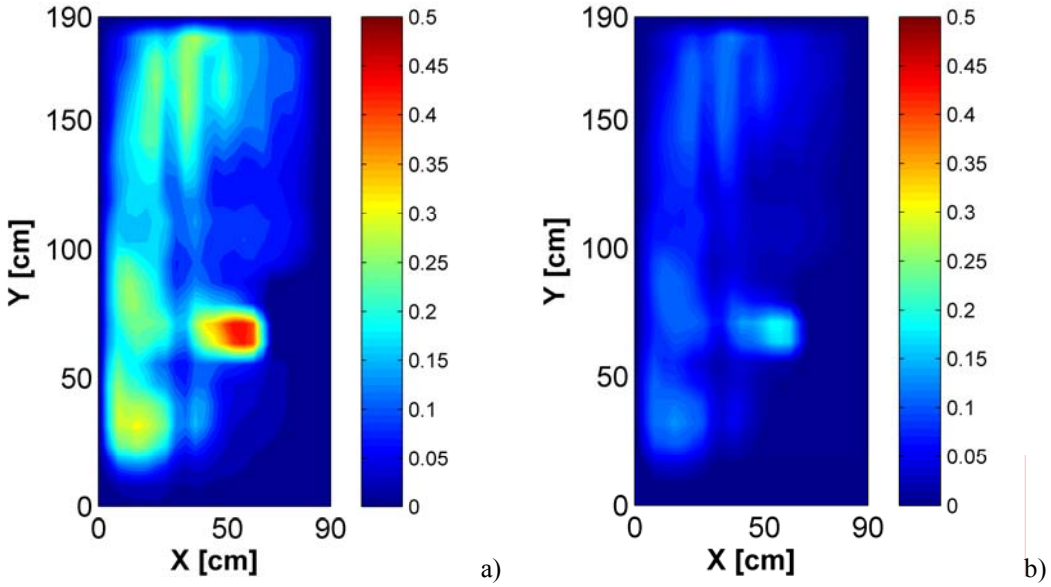

Figure 6 a) Raw holdup map. b) Hold up map after correction by Eqn.29.

As it can be seen, the final distribution is qualitatively consistent with results by Barigou and Greaves (1996) and is also significantly different from the uncorrected map. If the time averaged gas hold up of Fig.6b is further averaged over the entire plane, a realistic value of *0.04 %* is obtained. Clearly in order to get a more rigorous comparison with volume averaged data, the entire procedure should be repeated over several vertical planes placed at different angles with respect to baffles and proper volume weighed averages should be considered.

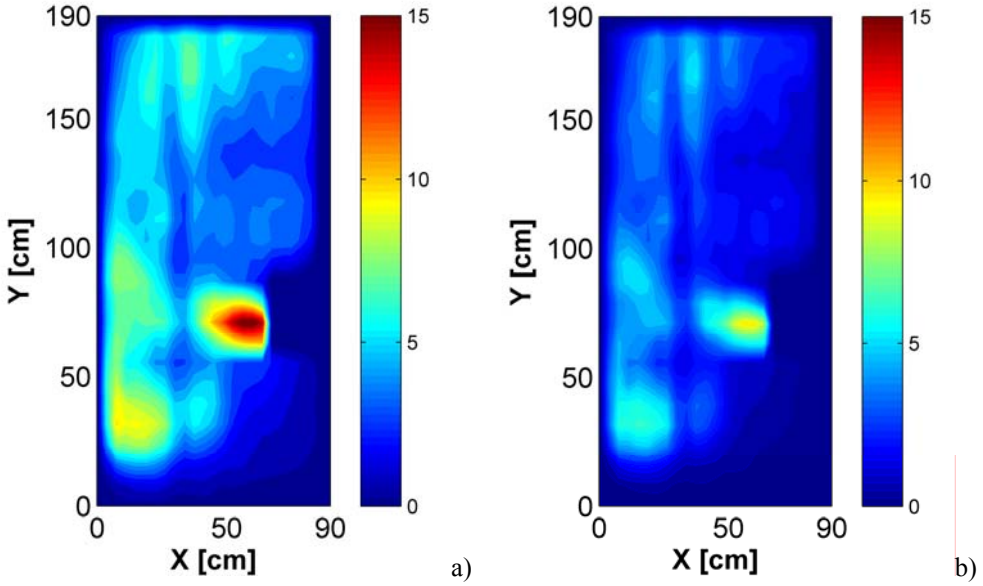

Figure 7 a) Raw specific interfacial area. b) Specific interfacial area after correction by Eqn.30.

The apparent local interfacial area map reported in Fig.7a was produced by applying the above described averaging procedure to local interfacial area raw data. After application of the relevant correction factor (Eqn.30) the final result reported in Fig.7b was obtained. If the time

averaged interfacial area of Fig.7b is further averaged over the entire plane, a value of $1.95\ m^{-1}$ is obtained. Once again, it can be seen that a quite large difference exists between raw and corrected local interfacial areas, so highlighting the need and importance of the correction. In the present case, this is clearly due to the fairly large laser sheet thickness (with respect to bubble size) adopted during data collection.

CONCLUSIONS

A novel technique has been developed for measuring local bubble properties in gas liquid dispersions. The technique is based on the use of a fluorescent liquid phase coupled with a laser sheet and a purposely developed digital image analysis routine. It may be regarded as being particularly reliable thanks to its ability to discard from the analysis visible, yet out-of-plane, bubbles. It can be conveniently employed for measuring local features of gas liquid dispersions, such as bubble size, gas hold-up and interfacial area, provided that sufficiently dilute dispersions are investigated. The technique viability was tested in the case of a gas-liquid stirred tank. The preliminary results obtained were found to be in good agreement with expectations.

REFERENCES

Aubin J., Le Sauze N., Bertrand J., Fletcher D.F., and Xuereb C., 2004. PIV measurements of flow in an aerated tank stirred by a down- and an up-pumping axial flow impeller. Experimental Thermal and Fluid Science, **28**, 447–456.

Barigou M. and Greaves M., 1992 Bubbles size distributions in a mechanically agitated gas-liquid contactor. Chem. Eng. Sci., **47**(8), 2009–2025.

Barigou M. and Greaves M., 1996. Gas holdup and interfacial area distributions in a mechanically agitated gas-liquid contactor. Chem. Eng. Res. Des., **74**, 397–405.

Boyer C., Duquenne A.M., and Wild G., 2002. Measuring techniques in gas-liquid and gas-liquid-solid reactors. Chem. Eng. Sci., **57**, 3185–3215.

Buffon, G., 1777. Essai d'arithmetique morale. Histoire Natureel 4A, 685.

Busciglio A., Grisafi F., Scargiali F., Brucato A., 2010. On the measurement of bubble size distribution in gas-liquid contactors via light sheet and image analysis, Chem. Eng. Sci. **65**, 2558-2568.

Busciglio A., Grisafi F., Scargiali F., Brucato A., 2010. On the measurement gas hold-up and interfacial area in gas-liquid contactors via light sheet and image analysis, in press on Chem. Eng. Sci.

Calderbank P.H., 1958. Physical rate processes in industrial fermentation. Part 1. the interfacial area in gas-liquid contacting with mechanical agitation. Trans. Inst. Chem. Engrs., **36**, 443–463.

Chung K., Simmons M., Barigou M., 2009. Local gas and liquid phase velocity measurement in a miniature stirred vessel using piv combined with a new image processing algorithm. Exp. Therm. Fluid Science, **33**, 743–753.

Clark N., Liu W., Turton R., 1996. Data interpretation techniques for inferring bubble size distribution from probe signals in fluidized systems. Powder Technol., **88**, 179–188.

Clark N., Turton R., 1988. Chord length distribution related to bubble size distributions in multiphase flow. Int. J. Multiphase Flow, **14**(4), 413–424.

Gunn D., Al-Doori H., 1985. The measurement of bubble flows in fluidized beds by electrical probe. Int. J. Multiphase Flow, **11**, 535–551.

Herringe R., Davis, M., 1976. Structural development of gas-liquid mixture flows. J. Fluid Mechs., **73**(1), 97–123.

Hobbel E., Davies R., Rennie F., Allen T., Butler L., Waters E., Smith J., Sylvester, R.W., 1991. Modern methods of on-line size analysis for particulate process streams. Part. Part. Syst. Charact., **8**, 29–34.

Khopkar A.R., Aubin J., Xuereb C., Le Sauze N., Bertrand J., and Ranade V.V., 2003. Gas-liquid flow generated by pitched-blade turbine: particle image velocimetry measurements and computational fluid dynamics simulations. Ind. Eng. Chem. Res., **42**, 5318–5332.

Laakkonen M., Honkanen M., Saarenrinn P., and Aittamaa J., 2005. Local bubble size distributions, gas-liquid interfacial areas and gas holdups in a stirred vessel with particle image velocimetry. Chemical Engineering Journal, **109**, 37–47.

Langston P., Burbridge A., Jones T., Simmons M., 2001. Particle and droplet size analysis from chord measurements using bayes' theorem. Powder Technol., **116**, 33–42.

Li M., Wilkinson D., 2005. Determination of non-spherical particle size distribution from chord length measuremens. part i: theoretical analysis. Chem. Eng. Sci., **60**, 3251–3265.

Li M., Wilkinson D., Patchingolla K., 2005. Determination of non-spherical particle size distribution from chord length measuremens. part ii: experimental validation. Chem. Eng. Sci., **60**, 4992–5003.

Liu Z., Zheng Y., Jia L., and Zhang Q., 2005. Study of bubble induced flow structure using PIV. Chemical Engineering Science, **60**, 3537–3552.

Liu W., Clark N., 1995. Relationship between distributions of chord lengths and distribution of bubble sizes including their statistical parameters. Int. J. Multiphase flow, **21**(6), 1073–1089.

Liu W., Clark N., Karamavruc A., 1996. General method for the transformation of chord length data to a local bubble size distribution. AIChE J., **42**(10), 2713.

Liu W., Clark N., Karamavruc A., 1998. Relationship between distributions bubble size distribution and chord length distribution in heterogeneously bubbling systems. Chem. Eng. Sci., **53**(6), 1267–1276.

Mandarim De Lacerda C., 2003. Stereological tools in biomedical research. An. Acad. Bras. Cienc., **75**(4), 469–486.

Montante G., Magelli F., and Paglianti A., 2007. Experimental analysis and computational modelling of gas-liquid stirred vessels. IChemE, **85**(A5), 647–653.

Ruf A., Worlitschek J., Mazzotti M., 2000. Modeling and experimental analysis of psd measurements through fbrm. Part. Part. Syst. Char., **17**, 167–179.

Russ J., Dehoff R., 1999. Practical Stereology, 2nd ed. Plenum Press, New York, NY.

Simmons M., Langston P., Burbridge A., 1999. Particle and drop size analysis from chord distribution. Powder Technol., **102**, 75–83.

Spicka P., Dias M.M., and Lopes J.S.B., 2001. Gas liquid flow in a 2D column: Comparison between experimental data and CFD modelling. Chem. Eng. Sci., **56**, 6367–6383.

Sridhar P., Potter O.E., 1980. Interfacial areas in gas-liquid stirred vessels. Chem. Eng. Sci., **35**(3):683–695.

Stroeven P., Hu J., 2006. Review paper - stereology: historical perspective and applicability to concrete technology. Materials and Structures, **39**, 127– 135.

Worlitschek J., Hocker T., Mazzotti M., 2005. Restoration of psd from chord length distribution data using the method of projection onto convex sets. Part. Part. Syst. Charact., **22**, 81–98.

Wynn, E., 2003. Relationship between particle-size and chord-length distributions in focused beam reflectance measurement: stability of direct inversion and weighting. Powder Technol., **133**, 125–133.